Snowball Earth Bifurcations in a Fully-Implicit Earth System Model

Thomas E. Mulder

Department of Mathematics and Computer Science,
University of Groningen, Groningen, The Netherlands

Institute for Marine and Atmospheric Research Utrecht,
Department of Physics and Astronomy, Utrecht University,
Utrecht, The Netherlands
t.e.mulder@rug.nl

Heiko Goelzer

NORCE Norwegian Research Centre,
Bjerknes Centre for Climate Research, Bergen, Norway

Institute for Marine and Atmospheric Research Utrecht,
Department of Physics and Astronomy, Utrecht University,
Utrecht, The Netherlands

Fred W. Wubs

Department of Mathematics and Computer Science,
University of Groningen, Groningen, The Netherlands

Henk A. Dijkstra

Institute for Marine and Atmospheric Research Utrecht and
Centre for Complex Systems Studies,
Department of Physics and Astronomy, Utrecht University,
Utrecht, The Netherlands

There is now much geological evidence that the Earth was fully glaciated during several periods in the geological past (about 700 Myr ago) and attained a so-called Snowball Earth (SBE) state. Additional support for this idea has come from climate models of varying complexity that show transitions to SBE states and undergo hysteresis under changes in solar radiation. In this paper, we apply large-scale bifurcation analyses to a novel, fully-implicit Earth System Model of Intermediate Complexity (I-EMIC) to study SBE transitions. The I-EMIC contains a primitive equation ocean model, a model for atmospheric heat and moisture transport, a sea ice component and formulations for the adjustment of albedo over snow and ice. With the I-EMIC, high-dimensional branches of the SBE bifurcation diagram are obtained through parameter continuation. We are able to identify stable and unstable equilibria and uncover an intricate bifurcation structure associated with the ice-albedo feedback. Moreover, large-scale linear stability analyses are performed near major bifurcations, revealing the spatial nature of destabilizing perturbations.

Keywords: Bifurcation analysis; snowball Earth; Earth system model.

1. Introduction

Glacial deposits that appeared to have formed in the tropics [Kirschvink, 1992] lead eventually to the idea that grounded ice sheets reached sea level at all latitudes during two long-lived glaciations in the so-called Cryogenian (718–635 Myr). A comprehensive review [Hoffman *et al.*, 2017] describes most of the current knowledge of the climate dynamics and the geology–geobiology of the corresponding "Snowball Earth" (SBE) states.

Transitions to SBE conditions are already present in simple energy balance models (EBMs) that simulate an ice-albedo feedback [Ghil & Childress, 1987]. Moreover, numerical simulations with models of higher complexity show the existence of a similar bifurcation structure and hysteresis behavior [Abbot *et al.*, 2011; Voigt *et al.*, 2011; Yang *et al.*, 2012a, 2012b]. Several models with varying topography configurations show the existence of SBE bifurcations. An aquaplanet (no continents) is used in [Abbot *et al.*, 2011], where additional intermediate steady states are found with a small strip of open ocean around the equator. In [Voigt *et al.*, 2011] the bifurcation points are investigated for a more realistic Marinoan topography and present-day topographies are used in [Yang *et al.*, 2012a, 2012b]. Global glaciations have also been found in the study of Earth-like climates [Boschi *et al.*, 2012].

To understand the spatial patterns associated with SBE transitions, bifurcation analyses of spatially extended models (i.e. described by PDEs) is needed. Here, we build on the fully-implicit primitive equation ocean model THCM [Dijkstra *et al.*, 2001; de Niet *et al.*, 2007] to develop a novel Implicit Earth System Model of Intermediate Complexity (I-EMIC). Apart from the ocean model THCM, the I-EMIC contains models of sea ice, atmospheric heat and humidity transport, evaporation, precipitation and albedo adjustments. The challenge here is to construct a model suitable for continuation methods, where one needs to avoid *ad-hoc* procedures, i.e. hard on-off switches of physical mechanisms that break the differentiability of the discrete equations. In particular, switches in forcing due to changes in local state characteristics cannot be instantaneous. Here, the general procedure to circumvent on-off selection is by letting an auxiliary, continuous "masking" field determine which forcing is applied.

With the I-EMIC, we create a more complete view of the SBE bifurcation diagram than what is currently available with limited time integrations. The implicit methodology allows the use of a continuation algorithm that tracks steady states under changes in incoming solar radiation. At bifurcation points, the algorithm continues into the unstable regime, where spatial patterns of the destabilizing perturbations can be obtained through eigenvalue analyses. As in [Yang *et al.*, 2012b], we will identify the bifurcation points for a model configuration with a present-day topography.

In Sec. 2, we present the components of the I-EMIC. Details on the implementation and coupling of the components are given in Sec. 3. Details on the numerical methods used are presented in Sec. 4. In Sec. 5, we compute bifurcation diagrams using numerical continuations in radiative forcing. The major SBE bifurcations are identified, including the destabilizing perturbation patterns that explain the transition from and to a SBE state. We conclude with a summary and discussion in Sec. 6.

2. Components of the I-EMIC

Central to the I-EMIC is the fully-implicit ocean model THCM [Dijkstra *et al.*, 2001]. The added geophysical components are implicit adaptations of models presented in [Gildor & Tziperman, 2001; Fanning & Weaver, 1996; Weaver *et al.*, 2001] and couple to the temperature and salinity equations in THCM. In this section we will provide the model equations in their dimensional form. An overview of the model equations and a list of the relevant parameter values are given in Appendices A and B, respectively.

2.1. *The ocean model*

The ocean component of the I-EMIC is the fully-implicit thermohaline circulation model THCM, originally described in [Dijkstra *et al.*, 2001]. The model has been adapted through the years with an improved grid configuration [Wubs *et al.*, 2006], tailored preconditioning [de Niet *et al.*, 2007], improved mixing representations [de Niet *et al.*, 2007; den Toom *et al.*, 2011] and a parallelization strategy [Thies *et al.*, 2009]. As the equations have been presented and discussed elsewhere, we only describe the main aspects of the model and provide the full equations in Appendix A.

The primitive equations are formulated using spherical coordinates (ϕ, θ, z) restricted to a domain $\phi \in [\phi_W, \phi_E]$, $\theta \in [\theta_S, \theta_N]$ and $z \in [-H_o, 0]$, that is

rotating with angular velocity Ω. Here, H_o is the maximum ocean depth and the atmosphere-ocean interface at $z = 0$ is rigid. Additional boundaries within the domain are introduced using a land mask $M(\phi, \theta, z) \in [0, 1]$ that describes the bathymetry and, hence, a more detailed flow domain. Note that in the experiments in Sec. 5 we consider a global configuration and let the zonal boundaries ϕ_W and ϕ_E become periodic.

Horizontal velocities are given by u in the longitudinal and v in the latitudinal direction. Vertical velocity, pressure, temperature and salinity are indicated by w, p, T and S, respectively. The governing equations use the hydrostatic and Boussinesq approximations and are shown in Appendix A, Eqs. (A.1)–(A.6). Mixing of momentum is represented by eddy diffusivities, where A_H and A_V are the horizontal and vertical friction coefficients. The coefficients K_H and K_V determine the horizontal and vertical diffusivities of heat and salt. A linear equation of state is used, with expansion coefficients α_T and α_S. In Table B.1 an overview is given of the relevant ocean parameters. The horizontal velocity field is driven by a wind stress $(Q_\tau^\phi, Q_\tau^\theta)$, that is applied as a body forcing over the upper layer.

In the temperature and salinity equations, continuous convective adjustment terms, ca$(\cdot)$, are introduced to locally remove static instabilities using strong vertical mixing of heat and salinity [den Toom *et al.*, 2011]. Driving terms for heat and salinity are provided by surface fluxes Q_T and Q_S that depend on the atmosphere and sea ice state. Similar to the wind stress field, the fluxes Q_T and Q_S are applied as body forcings over the upper layer (see Sec. 3).

At the bottom and surface boundaries we apply slip conditions for the horizontal velocities, impose no flow conditions on the vertical velocity and require heat and salinity fluxes to be zero [see (A.20)–(A.22)]. At the lateral boundaries we impose no-slip conditions on the velocities and zero-flux conditions on heat and salinity. In a global configuration the zonal boundaries are replaced by periodicity constraints, i.e. when $\phi_W = \phi_E$, we require that $u(\phi_W) = u(\phi_E)$, $v(\phi_W) = v(\phi_E)$, $w(\phi_W) = w(\phi_E)$, $T(\phi_W) = T(\phi_E)$ and $S(\phi_W) = S(\phi_E)$.

2.2. *The atmosphere model*

The atmosphere equations in the I-EMIC are based on the energy-moisture balance model in [Fanning & Weaver, 1996]. The state of the atmosphere component contains atmospheric temperature T^a, specific humidity q, albedo α and the global mean precipitation $\overline{P}$. The evolution of T^a and q is governed by vertically integrated energy balance models, with a linear Budyko–Sellers-type parameterization of outgoing longwave radiation Q_{LW} [Budyko, 1969]. We let adjustments in albedo α depend on surface type and temperature. The full parameterization of α is discussed separately in Sec. 2.5. Precipitation is included through a spatial distribution function d combined with a mean precipitation $\overline{P}$, which is computed through an auxiliary integral equation.

The two-dimensional energy balance equations are formulated using spherical coordinates (ϕ, θ), restricted to $\phi \in [\phi_W, \phi_E]$ and $\theta \in [\theta_S, \theta_N]$. At the lateral boundaries we require no flux conditions [see (A.23)–(A.24)]. In a global configuration we let $\phi_W = \phi_E$, which leads to requiring $T^a(\phi_W) = T^a(\phi_E)$ and $q(\phi_W) = q(\phi_E)$.

The vertically integrated temperature T^a is subject to horizontal diffusive heat transport, Q_D, and driven by a balance of radiative forcings containing outgoing longwave radiation Q_{LW}, net shortwave radiation Q_{SW}, sensible heat flux Q_{SH} and a latent heat flux due to precipitation Q_{LH}:

$$\rho_a H_a C_{pa} \frac{\partial T^a}{\partial t} = Q_D - Q_{LW} + Q_{SW} + Q_{SH} + Q_{LH},$$
$$Q_D = \rho_a H_a C_{pa} D_0 \nabla_h \cdot (D(\theta) \nabla_h T^a), \tag{1}$$

where ρ_a denotes atmospheric density, H_a the integration scale height and C_{pa} the specific heat of air. The latitudinal dependence on, and magnitude of eddy diffusivity are controlled by $D(\theta)$ and D_0, where

$$D(\theta) = 0.9 + 1.5e^{-12\theta^2/\pi}. \tag{2}$$

The radiative forcing terms are given by

$$Q_{LW} = A + BT^a, \tag{3}$$

$$Q_{SW} = \frac{\Sigma_0}{4} S(\theta)(1 - \alpha)(1 - C_0), \tag{4}$$

$$Q_{SH} = \mu(T^s - T^a), \tag{5}$$

$$Q_{LH} = \rho_o L_v P. \tag{6}$$

Here, we use a linear outgoing longwave radiative flux Q_{LW}, with coefficients A and B [Budyko, 1969]. The shortwave radiation Q_{SW} is determined by

the solar constant Σ_0, albedo α and atmospheric absorption $1 - C_0$. A latitudinal dependence is introduced through $S(\theta)$ [North *et al.*, 1981]:

$$S(\theta) = 1 - \frac{0.482(3\sin^2(\theta) - 1)}{2}. \qquad (7)$$

In the sensible heat flux Q_{SH}, T^s denotes the temperature of the underlying surface and we use a simplified exchange coefficient $\mu = \rho_a C_{pa} C_H |V_a|$, where C_H is the Stanton number and $|V_a|$ the mean surface wind speed. The latent heat flux Q_{LH} depends on precipitation P (12), and is computed using the reference water density ρ_o and latent heat of vaporization L_v.

The vertically integrated specific humidity q is subject to diffusive horizontal transport and driven by the difference between evaporation and precipitation $E - P$ [Fanning & Weaver, 1996; Weaver *et al.*, 2001]:

$$\rho_a H_q \frac{\partial q}{\partial t} = \rho_a H_q \nabla_h \cdot (\kappa \nabla_h q) + \rho_o(E - P), \qquad (8)$$

where H_q is the integration scale height for specific humidity and κ the eddy diffusivity. Evaporation E is calculated from

$$E = \eta(q_{\text{sat}}(T^s) - q), \quad \text{with } \eta = \frac{\rho_a C_E |V_a|}{\rho_o}. \qquad (9)$$

Here, C_E is the Dalton number and $q_{\text{sat}}(T^s)$ the saturation humidity that depends on the underlying surface type [Weaver *et al.*, 2001], see Sec. 3.3. In Table B.2 an overview of all atmosphere parameters with their dimensions and typical values is given.

Precipitation is obtained through an additional constraint on the $E - P$ difference that ensures that all evaporated water is returned through precipitation:

$$\int (E - P)dA = 0, \qquad (10)$$

where A denotes the ocean surface. The total mean precipitation is then given by

$$\overline{P} = \frac{1}{A} \int E \, dA. \qquad (11)$$

To incorporate spatial features of the precipitation field a distribution function d is introduced, giving

$$P = \overline{P} d(\phi, \theta), \qquad (12)$$

with the function d chosen such that (10) is satisfied, i.e.

$$\frac{1}{A} \int d(\phi, \theta)dA = 1. \qquad (13)$$

The mean precipitation $\overline{P}$ is added to the atmosphere model as an auxiliary unknown. An additional integral equation given by (11) is then added to close the system of equations. The distribution function d is implemented stationary, but can be chosen freely as long as (13) holds. This implies that precipitation/snowfall on land can be represented (P is allowed to be nonzero above land) but, without runoff, this is only useful in the parameterization of reflectivity α (Sec. 2.5).

2.3. Land temperature

The heat flux from the atmosphere into the land, Q_T^{la}, depends on the reflectivity α, the atmospheric temperature T^a and the land temperature T^l:

$$Q_T^{la} = Q_{SW} - Q_{SH}, \qquad (14)$$

with

$$Q_{SW} = \frac{\Sigma_0}{4} S(\theta)(1 - \alpha)C_0,$$

$$Q_{SH} = \mu(T^l - T^a),$$

where we reuse the radiative flux notations in the context of heat fluxes over land [cf. (4) and (5)]. For simplicity, we let the heat capacity of land be zero, which leads to zero heat flux from the atmosphere into the land, i.e. $Q_T^{la} = 0$. Land temperature can therefore be written as a function of atmospheric temperature and albedo:

$$T^l = T^a + \frac{\Sigma_0}{4\mu} S(\theta)(1 - \alpha)C_0. \qquad (15)$$

We do not append T^l to the model unknowns and this expression is not added to the system of atmosphere equations, but substituted where needed.

2.4. The sea ice model

The sea ice component is an implicit formulation of the thermodynamic sea ice model in [Weaver *et al.*, 2001], where a number of additional unknowns are introduced to ease submodel interactions. An evolution equation for sea ice thickness H is solved, together with three algebraic constraints that compute the sea ice-atmosphere heat flux Q_T^{sa},

a continuous sea ice mask M^{si} and the sea ice surface temperature T^i. The mask equation is added to simplify sea ice-dependent derivatives by representing the (possibly fractional) presence of sea ice at a grid point.

The evolution of sea ice thickness is governed by

$$\rho_i L_f \frac{\partial H}{\partial t} = Q_T^{os} - Q_T^{sa} - \rho_o L_f E, \qquad (16)$$

where the difference $Q_T^{os} - Q_T^{as}$ is the heat flux available for the creation of sea ice, ρ_i is the ice density, L_f is the latent heat of fusion of ice and E is sublimation. The heat flux directed from the sea ice into the ocean Q_T^{os} depends on the (salinity dependent) freezing point of ocean water T^f and the ocean surface layer temperature T^o (which we distinguish from the full 3D ocean temperature state T):

$$Q_T^{os} = \zeta(T^f - T^o), \quad \text{with } \zeta = C_s u_\tau \rho_o C_{po}. \quad (17)$$

Here, C_{po} is the specific heat of sea water, u_τ is the skin friction velocity and C_s is a relaxation parameter.

The heat flux from the atmosphere into the sea ice, Q_T^{sa}, is given by

$$0 = Q_T^{sa} - Q_{SW} + Q_{SH} + Q_{LH}, \qquad (18)$$

with

$$Q_{SW} = \frac{\Sigma_0}{4} S(\theta)(1 - \alpha) C_0,$$

$$Q_{SH} = \mu(T^i - T^a),$$

$$Q_{LH} = \rho_o L_s E.$$

Here, Q_{SW} is the incoming shortwave radiation, the sensible heat flux Q_{SH} is calculated with sea ice surface temperature T^i, Q_{LH} is the latent heat flux due to sublimation and L_s is the latent heat of sublimation of ice. The heat flux Q_T^{sa} is added to the sea ice model state and the corresponding algebraic constraint (18) is added to the system of equations.

Equating the sea ice-atmosphere flux with the conductive flux through the ice, results in an expression for the sea ice surface temperature T^i [Weaver *et al.*, 2001]:

$$0 = T^f(S) - T^i + \frac{Q_T^{sa} H}{I_c}, \qquad (19)$$

with I_c denoting the thermal conductivity of ice. The surface temperature T^i is added as a model

state component, which leads to the addition of (19) to the system of equations.

Finally, an equation for the sea ice mask M^{si} is added:

$$0 = M^{si} - \frac{1}{2}\left[1 + \tanh\left(\frac{H - \tau_s}{\epsilon}\right)\right], \qquad (20)$$

with τ_s a threshold ice thickness and ϵ a transition width that may represent subgrid sea ice fractions. See Table B.3 for an overview of the sea ice specific parameters and their values.

The resulting sea ice model state contains the unknowns $(H, Q_T^{sa}, M^{si}, T^i)$ with the following governing system of equations:

$$\rho_i L_f \frac{\partial H}{\partial t} = Q_T^{os} - Q_T^{sa} - \rho_o L_f E, \qquad (21)$$

$$0 = Q_T^{sa} - Q_{SW} + Q_{SH} + Q_{LH}, \qquad (22)$$

$$0 = M^{si} - \frac{1}{2}\left[1 + \tanh\left(\frac{H - \tau_s}{\epsilon}\right)\right], \quad (23)$$

$$0 = T^f - T^i + \frac{Q_T^{sa} H}{I_c}. \qquad (24)$$

2.5. *The albedo model*

The reflectivity α, present in the incoming shortwave radiation fluxes, depends on the type of underlying surface. For atmosphere points above ocean and sea ice this can be written as a straightforward dependence on the continuous sea ice mask $M^{si} \in [0, 1]$. On land we need a parameterization for the occurrence of snow and ice that depends on land temperature T^l and precipitation P. We let albedo evolve according to

$$\frac{\partial \alpha}{\partial t} = \begin{cases} \tau_f^{-1}(\alpha_0 + \Delta\alpha f(T^l, P) - \alpha) \\ \quad \text{above land points,} \\ \tau_c^{-1}(\alpha_0 + \Delta\alpha M^{si} - \alpha) \\ \quad \text{above ocean or sea ice points,} \end{cases} \qquad (25)$$

with restoring timescales τ_f, τ_c, a mean background value α_0 and an excursion $\Delta\alpha$. The function $f(T^l, P) : \mathbb{R} \times \mathbb{R} \to [0, 1]$ combines parameterization for melt, accumulation and the ratio of snow and liquid precipitation:

$$f(T^l, P) = \mathcal{H}(T_m - T^l, \epsilon_m)\mathcal{H}(P - P_a, \epsilon_a)$$
$$\times \mathcal{H}(T_r - T^l, \epsilon_r) \qquad (26)$$

with

$$\mathcal{H}(x, \epsilon) = \frac{1}{2}\left[1 + \tanh\left(\frac{x}{\epsilon}\right)\right]. \qquad (27)$$

The center and width of the switching behavior in the approximate Heaviside functions $\mathcal{H}$ are given by (ϵ_m, T_m) for melting, (ϵ_a, P_a) for accumulation and (ϵ_r, T_r) for the snow/rain ratio. Melt transitions smoothly from year-round ice cover to year-round ice free conditions. Accumulation and the snow/rain ratio require a sharper switch at their critical values. We let albedo α be an additional state component of the atmosphere model and add the evolution equation (25) to the atmosphere system.

3. Coupling Details

In this section we describe the heat and freshwater fluxes that are communicated between the components of the I-EMIC. The coupled model setup is such that the state of one component becomes the forcing of another one, with minimal adjustments. For instance, the fluxes into the ocean are calculated using internal (ocean) and external (atmosphere or sea ice) states. We only communicate state components and let submodels construct fluxes independently. In this way, derivatives with respect to all unknowns (internal and external) are readily available at the model level. In most cases this is a natural implementation. It does, however, imply that some fluxes are computed multiple times at different locations.

The I-EMIC contains two different masks that determine the type of fluxes for the submodel interactions. A fixed, three-dimensional land mask $M \in [0, 1]$ describes the ocean bathymetry with discrete values: $M = 1$ on land and $M = 0$ elsewhere. Then there is an evolving, two-dimensional sea ice mask $M^{si} \in [0, 1]$ that depends continuously on sea ice thickness H, see Sec. 2.4. With sufficient sea ice cover, $M^{si} \approx 1$. A critical sea ice thickness will trigger a change in flux interactions between the submodels. By adding M^{si} to the list of sea ice unknowns, we let a state component control flux changes directly and, thereby, simplify flux derivatives.

3.1. *Forcing of oceanic temperature and salinity*

The forcing in the oceanic temperature equation, Q_T in (A.5), is a combination of atmospheric and sea ice heat fluxes (ignoring geothermal heat fluxes) that are applied to the ocean's upper layer:

$$Q_T = \frac{g(z)}{\rho_o C_{po} H_m}(Q_T^{oa}(1 - M^{si}) + M^{si}Q_T^{os}), \quad (28)$$

where H_m is the upper layer depth, Q_T^{oa} the heat flux from the atmosphere into the ocean, Q_T^{os} the heat flux from the sea ice into the ocean [as given by (17)] and $M^{si} \in [0, 1]$ the sea ice mask. The body forcing uses a vertical distribution $g(z)$, which equals 1 in the upper layer and 0 elsewhere.

The heat flux from the atmosphere into the ocean contains incoming shortwave radiation Q_{SW}, a sensible heat flux Q_{SH} and a latent heat flux due to evaporation Q_{LH}:

$$Q_T^{oa} = Q_{SW} - Q_{SH} - Q_{LH}, \qquad (29)$$

with

$$Q_{SW} = \frac{\Sigma_0}{4}S(\theta)(1 - \alpha)C_0,$$

$$Q_{SH} = \mu(T^o - T^a),$$

$$Q_{LH} = \rho_o L_v E.$$

The forcing Q_S of the salinity equation (A.6) is given by the ocean-atmosphere freshwater flux Q_S^{oa} and the ocean-sea ice brine and melt flux Q_S^{os}, which are combined through the sea ice mask M^{si} and applied to the upper layer of the ocean:

$$Q_S = \frac{g(z)S_0}{H_m}((1 - M^{si})Q_S^{oa} + M^{si}Q_S^{os} - \gamma). \quad (30)$$

Here, γ is an integral correction such that $\int Q_S dA = 0$, which ensures conservation of salt. In Sec. 3.2, it is shown that γ compensates for a lack of physical mechanisms represented by the ocean-sea ice freshwater flux Q_S^{os}. The ocean-atmosphere freshwater flux Q_S^{oa}, directed into the ocean, is the evaporation-precipitation difference

$$Q_S^{oa} = E^o - P, \qquad (31)$$

where evaporation over ocean points E^o is a function of the ocean surface temperature T^o and specific humidity q in the atmosphere (9). Precipitation P is computed according to (12). The salinity flux due to brine rejection and melting is [Weaver *et al.*, 2001]

$$Q_S^{os} = \frac{Q_T^{os} - Q_T^{sa}}{\rho_o L_f}. \qquad (32)$$

To summarize, the ocean submodel depends on all state components of the atmosphere model: T^a,

q, α and $\overline{P}$. Of the sea ice model, only the unknown flux Q_T^{sa} and mask M^{si} are needed, as the flux Q_T^{os} can be computed from oceanic state components. However, an additional correction factor γ to guarantee salinity conservation is also required, which we discuss in the next section.

3.2. *Buoyancy flux correction*

The salinity flux due to brine rejection and melting, Q_S^{os}, adds to the otherwise closed salinity budget. In the total buoyancy flux Q_S (30) this leads to a correction term γ in order to satisfy the conservation of salt. Note that, without sea ice, the flux Q_S does satisfy this conservation requirement due to (10). Taking the integral of (30) over the ocean surface and setting it to zero leads to an expression for γ:

$$\gamma A = \int Q_S^{oa} dA - \int M^{si} Q_S^{oa} dA$$
$$+ \int M^{si} Q_S^{os} dA. \tag{33}$$

Using (31) we write

$$\int Q_S^{oa} dA = \int E^o dA - \overline{P} A, \tag{34}$$

where E^o is the evaporation at ocean points (see Sec. 3.3) and $\overline{P}$ is the global mean precipitation (11) which satisfies the integral equation:

$$\overline{P} A = \int E^o dA + \int M^{si} (E^i - E^o) dA, \tag{35}$$

where we distinguish between evaporation over ocean points E^o and sublimation over sea ice points E^i. Substituting (35) in (34) gives

$$\int Q_S^{oa} dA = \int M^{si} (E^o - E^i) dA. \tag{36}$$

A part of the atmospheric buoyancy flux is blocked by the sea ice. Integrated over the sea ice area the blocked flux is given by

$$\int M^{si} Q_S^{oa} dA = \int M^{si} (E^o - P) dA. \tag{37}$$

Using (36) and (37), the correction equation (33) reduces to

$$\gamma A = \int M^{si} (Q_S^{os} - (E^i - P)) dA. \tag{38}$$

Hence, physically, the correction γ originates from the difference between the net buoyancy fluxes at the top and bottom of the floating sea ice. This correction therefore compensates for the lack of additional physical mechanisms, e.g. precipitation and runoff.

3.3. *Forcing of the atmosphere*

The atmosphere model depends on the underlying surface type and surface temperature T^s, which influences sensible heat fluxes, albedo and evaporation/sublimation. The surface temperature T^s is given by

$$T^s = \begin{cases} T^l & \text{if } M = 1 \\ & \quad \text{(land surface temperature),} \\ T^i & \text{if } M^{si} = 1 \\ & \quad \text{(sea ice surface temperature),} \\ T^o & \text{elsewhere} \\ & \quad \text{(ocean surface temperature).} \end{cases} \tag{39}$$

With the mask fields and different surface types incorporated, the sensible heat flux (5) expands to

$$Q_{SH} = \begin{cases} \mu(T^l - T^a) & \text{if } M = 1, \\ \mu(T^o[1 - M^{si}] + T^i M^{si} - T^a) \\ & \qquad \text{elsewhere.} \end{cases} \tag{40}$$

The latent heat flux (6) depends on the mean precipitation $\overline{P}$, which is given by (11). The evaporative term in (11) and (8) is expanded with the different surface types:

$$\overline{P} = \frac{1}{A} \int E dA = \frac{1}{A} \int (E^o(1 - M^{si}) + M^{si} E^i) dA, \tag{41}$$

with

$$E^o = \eta(q_{\text{sat}}(T^o) - q), \tag{42}$$

$$E^i = \eta(q_{\text{sat}}(T^i) - q), \tag{43}$$

where the saturation humidity q_{sat} for different surface types is given by

$$q_{\text{sat}}(T) = \begin{cases} c_1 \exp\left(\dfrac{c_2 T}{T + c_3}\right) & \text{if } T = T^i, \\ c_1 \exp\left(\dfrac{c_4 T}{T + c_5}\right) & \text{if } T = T^o. \end{cases} \tag{44}$$

The values of the saturation humidity coefficients are given in Table B.4.

4. Numerical Aspects

The ocean equations are discretized using a control volume discretization on an Arakawa B-grid in the horizontal [Arakawa & Lamb, 1977] and on a C-grid in the vertical direction. Earlier versions of THCM made use of a C-grid in the horizontal direction and suffered from numerical wiggles for small horizontal diffusivities A_H. In [Wubs *et al.*, 2006], it is shown that these numerical artifacts disappear when a B-grid is used in the horizontal direction. The unknowns of the other two-dimensional submodels couple with temperature and salinity at the cell-centers and are therefore also positioned at the cell-centers of a B-grid.

4.1. *Fixed point continuation*

Apart from a few transient computations we mainly use pseudo-arclength continuation [Keller, 1977] to obtain steady states for a range of control parameter values. After spatial discretization, the complete coupled problem (A.1)–(A.15) can be formulated as

$$B\dot{\mathbf{x}} = F(\mathbf{x}, \lambda), \qquad (45)$$

where $F : \mathbb{R}^n \times \mathbb{R} \to \mathbb{R}^n$ is a nonlinear operator given by the spatially discretized right-hand side of (A.1)–(A.15), λ denotes a control parameter and $\mathbf{x} \in \mathbb{R}^n$ is a vector containing n model unknowns. The matrix $B \in \mathbb{R}^{n \times n}$ controls the time derivatives in (A.1)–(A.15) and contains zero rows corresponding to algebraic constraints and integral equations. As B is singular, (45) is a system of differential-algebraic equations (DAEs).

Steady states of (45) satisfy

$$F(\mathbf{x}, \lambda) = 0. \qquad (46)$$

Fixed points $(\mathbf{x}, \lambda)$ lie on a curve that is naturally parameterized with an arclength parameter s: $\gamma(s) = (\mathbf{x}(s), \lambda(s))$. The curve satisfies a normalization constraint that closes the system:

$$\zeta \left\| \frac{d\mathbf{x}}{ds} \right\|_2^2 + (1 - \zeta)\left(\frac{d\lambda}{ds}\right)^2 = 1, \qquad (47)$$

where $\zeta \in (0, 1)$ is a positive tuning factor. The pseudo-arclength continuation algorithm follows a predictor-corrector procedure that is initialized with a known or trivial steady state. A new point on the curve is predicted and subsequently corrected in a Newton–Raphson root finding procedure [Press *et al.*, 2007]. The advantage of the arclength

parameterization is that when the Jacobian matrix of F becomes singular, the combined system (46) and (47) can still be solved. This allows the predictor-corrector procedure to continue through a bifurcation onto an unstable branch. See [Seydel, 2010] for a broad introduction into continuation techniques.

4.2. *Linear stability analysis*

The stability of points $(\mathbf{x}, \lambda)$ that satisfy (46) is investigated through a linear stability analysis. Consider a small perturbation of the steady state: $\mathbf{x} + \tilde{\mathbf{x}}$. Linearization of the perturbed system (45) around $\mathbf{x}$ gives an expression for the evolution of a local perturbation:

$$B\frac{d\tilde{\mathbf{x}}}{dt} = J(\mathbf{x}, \lambda)\tilde{\mathbf{x}}, \qquad (48)$$

where $J = \frac{\partial F}{\partial \mathbf{x}}$ is the Jacobian matrix of F. Solutions of (48) are of the form $\tilde{\mathbf{x}} = \hat{\mathbf{x}}e^{\sigma t}$, which gives a generalized eigenvalue problem:

$$\sigma B\hat{\mathbf{x}} = J(\mathbf{x}, \lambda)\hat{\mathbf{x}}. \qquad (49)$$

Local stability properties are then given by the eigenvalues σ and patterns of associated variability can be inferred from the eigenvectors $\hat{\mathbf{x}}$. For the large-scale linear stability problems in Sec. 5 we use the JDQZ generalized eigenvalue solver [Sleijpen *et al.*, 1996].

4.3. *Numerical coupling framework*

Submodels of the I-EMIC follow the monolithic formulation in (45). Next to a differentiable right-hand side F_i, the ith submodel also provides a Jacobian matrix $J_i = \frac{\partial F_i}{\partial \mathbf{x}_i}$, derivatives with respect to other submodel states $C_{ij} = \frac{\partial F_i}{\partial \mathbf{x}_j}$ and a suitable preconditioner for the Jacobian matrix, M_i, such that the conditioning of $M_i^{-1}J_i$ is better than that of J_i, and M_i is cheap to invert. The coupled Jacobian of the I-EMIC is given by

$$J = \begin{bmatrix} J_1 & C_{12} & \cdots & & C_{1m} \\ C_{21} & J_2 & & & \vdots \\ \vdots & & \ddots & & C_{m-1m} \\ C_{m1} & \cdots & C_{mm-1} & & J_m \end{bmatrix}. \qquad (50)$$

The system of equations $J\delta\mathbf{x} = \mathbf{b}$ is solved several times in the Newton corrector step of the arclength

continuation. Here we use flexible GMRES [Saad, 1993] on the full (monolithic) problem with right preconditioning. The coupled preconditioner M consists of the submodel preconditioners M_i, combined with the coupling blocks C_{ij}. Inversion of M is then performed with a few (backward or forward) block Gauss–Seidel iterations [Saad, 2003], allowing a partitioned preconditioning approach. The action $\mathbf{z} = M^{-1}\mathbf{v}$, for instance, can be approximated by the following forward Gauss-Seidel iteration:

$$
\begin{bmatrix}
M_1 & 0 & \cdots & 0 \\
C_{21} & M_2 & & \vdots \\
\vdots & & \ddots & \\
C_{m1} & \cdots & C_{mm-1} & M_m
\end{bmatrix}
\mathbf{z}^k
$$

$$
=
\begin{bmatrix}
0 & C_{12} & \cdots & C_{1m} \\
0 & 0 & & \vdots \\
\vdots & & \ddots & C_{m-1m} \\
0 & \cdots & & 0
\end{bmatrix}
\mathbf{z}^{k-1} + \mathbf{v}. \quad (51)
$$

5. Snowball Earth Bifurcations

We will use the full model (A.1)–(A.15) to compute a bifurcation diagram with the solar constant as control parameter. First, we compute stable stationary states through an implicit spinup, i.e. through time integration. Then, we apply a parameter continuation procedure to compute branches of steady states versus the solar constant.

The computations are performed for the fully coupled problem. We use a computational grid with a resolution of approximately $4°$ in both horizontal directions. In the vertical direction we use 12 layers with refinements towards the surface, such that the upper and bottom layers are $72\,\mathrm{m}$ and $858\,\mathrm{m}$ deep, respectively. For simplicity and computational efficiency we use a flat bottom ocean depth of $5000\,\mathrm{m}$ and a large horizontal eddy viscosity of $A_H = 1.6 \times 10^7 \,\mathrm{m}^2\mathrm{s}^{-1}$. The horizontal domain is periodic in the zonal direction and bounded by latitudes $[\theta_S, \theta_N] = [85.5°\mathrm{S}, 85.5°\mathrm{N}]$. Within the computational domain, the lateral boundaries are provided by a present-day topography mask.

Steady states are computed for two different physical setups. In setup (a), the ocean dynamics

are fully disabled. In setup (b) the ocean is driven by an idealized wind stress $(Q_\tau^\phi, Q_\tau^\theta)$, and heat fluxes Q_T from the atmosphere and sea ice components (28). Freshwater fluxes Q_S are ignored and the wind stress contains only a zonal component, given by the analytical profile in [Bryan, 1987]. The solar constant, present in the shortwave radiation terms Q_{SW}, is adjusted through $\lambda_\Sigma \Sigma_0$, where λ_Σ acts as the control parameter with $\lambda_\Sigma = 1$ for the default configuration. Figure 1 shows branches of steady states under changing λ_Σ for both setups. On the y-axis the total sea ice cover $A^{si} = \int M^{si} dA$, scaled with the total ocean surface A, is taken as a state indicator.

The continuations are started at steady states achieved through transient computations at $\lambda_\Sigma = 0.98$. As time stepping scheme, we use backward Euler with an adaptive time step that depends on the number of Newton iterations. The transients give steady states at points P_1^a and P_1^b for setups (a) and (b), respectively. From these points continuations in λ_Σ are performed in both directions along the branch of steady states. This procedure is repeated for both configurations at $\lambda_\Sigma = 0.94$, where transients end up in the fully ice-covered snowball state [left endpoint of the upper curve in Fig. 1(a)]. From here, continuations are only performed in the direction of increasing λ_Σ. For a dynamic ocean (configuration (b)) another transient to steady state is computed for $\lambda_\Sigma = 0.975$, and continuations in both directions of λ_Σ are performed [see orange curve in Fig. 1(c)]. Due to the high computational cost involved with traversing the complicated branches, most continuations remain incomplete and our focus lies on sections of the bifurcation diagram near the important bifurcations.

The continuation, starting at P_1^a and in the direction of decreasing λ_Σ, reaches a snowball Earth bifurcation at L_1^a. This can be verified with transients in a neighborhood of L_1^a, but we choose to solve the eigenvalue problem (49) at points before and after the saddle-node bifurcation. With this approach we find that, at L_1^a, an eigenvalue crosses the imaginary axis. The snowball Earth bifurcation for setup (b) is located at L_1^b. Here, eigenvalue solutions remain inconclusive (as the JDQZ solver fails to converge) and verification is done through the computation of transients. Both configurations reach the second snowball Earth bifurcation L_2, starting from P_2 in the direction of increased λ_Σ.
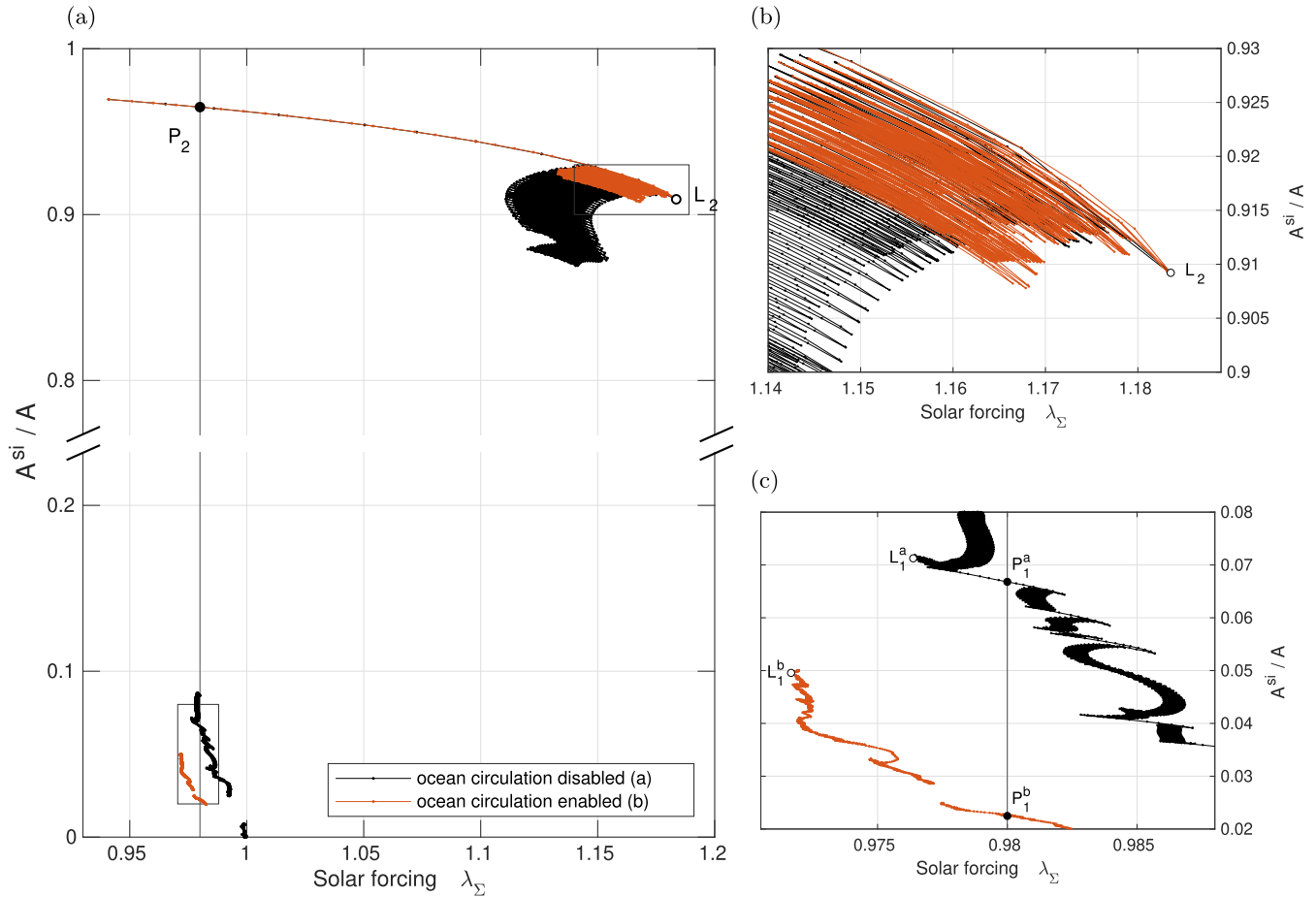
Fig. 1. (a) Complete and (b) and (c) zoomed-in views of the I-EMIC bifurcation diagram with solar forcing $\lambda_\Sigma \Sigma_0$. Default conditions are given by $\lambda_\Sigma = 1.0$. The points L_1^* and L_2 are the first and second critical snowball Earth bifurcations. In the multiple equilibria regime with sea ice present, we select points P at $\lambda_\Sigma = 0.98$. The ocean circulation is disabled (enabled) at P_1^a (P_1^b). In the SBE branch, at P_2, both configurations coincide. (b) Zoom-in of the region around the L_2 bifurcation. (c) Zoom-in of the region containing bifurcations L_1^a, L_1^b and points P_1^a, P_1^b.

Eigenvalue solves for both configurations show an eigenvalue crossing the imaginary axis at L_2.

The sea ice thickness and temperature state components of the coupled problem at P_1^a and P_1^b are depicted in Fig. 2. The sea ice thickness fields [Figs. 2(a) and 2(b)] show that sea ice extent is severely reduced by the existence of advective heat transport. Heat is transported to higher latitudes and prevents the formation of sea ice. The warmer ocean surface at high latitudes and the reduced reflectivity due to a lack of sea ice, contribute to a warmer atmosphere [Fig. 2(d)]. A stabilizing feedback loop is closed by considering that the warmer atmosphere at P_1^b keeps the ocean surface temperature above freezing values. The effect of enhanced oceanic heat transport is also visible from the position of the saddle-node bifurcations L_1^a and L_1^b: the snowball Earth bifurcation occurs for lower

incoming shortwave radiation and with less sea ice cover in configuration (b).

Density-driven ocean flows are enabled in configuration (b), which leads to advective transport of heat through overturning circulations. Figure 3 shows the meridional overturning circulation at the fixed points P_1^b and L_1^b, where the top panels display the global overturning circulations and the bottom panels their respective Atlantic components with Northern sinking profiles [Figs. 3(c) and 3(d)]. At the bifurcation L_1^b, the global overturning pattern persists [Fig. 3(b)], compared to P_1^b [Fig. 3(a)], with a similar positive and negative amplitude. Figure 4 shows the sea ice extent, sea surface- and atmospheric temperature at the two bifurcations L_1^a and L_1^b. The atmospheric temperature distribution at L_1^b [Fig. 4(d)] is similar to that at the bifurcation L_1^a [Fig. 4(c)], where no ocean circulations exist. At L_1^a,

(a)

(b)

(c)

(d)

Fig. 2. (a) and (b) Sea ice thickness (colors, in m) and sea surface temperature (contours, in $°$C). (a) Without ocean circulation at P_1^a (see Fig. 1) and (b) with ocean circulation enabled at P_1^b. (c) and (d) Atmospheric temperature in $°$C at the points (c) P_1^a and (d) P_1^b.

sea ice is well established in the Southern Ocean and is almost constant in the zonal direction, which is not the case at L_1^b. Ocean circulations inhibit sea ice growth and lead to a smaller sea ice extent and more spatial variation in sea ice cover at the snowball bifurcation.

The snowball states at P_2 and L_2 are shown in Fig. 5. In a fully ice-covered ocean, the surface temperature is restored to the local freezing temperature of sea water, according to (17). Hence, during the transition to a snowball state, the temperature-driven overturning circulation breaks down. Also, when $Q_S = 0$, the sea surface temperature is approximately homogeneous in the snowball state at P_2 [Fig. 5(a)], which explains why the bifurcation point L_2 is independent of the chosen setup.

(a)

(b)
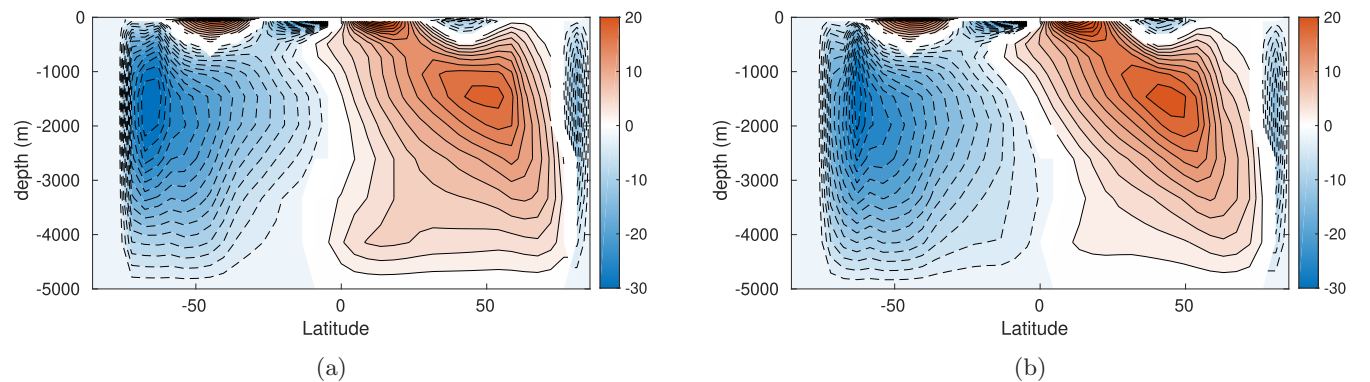
Fig. 3. (a) and (b) Global and (c) and (d) Atlantic meridional overturning streamfunction in Sv at points at (a) and (c) P_1^b and (b) and (d) L_1^b. The colorbar is based on streamfunction values below 1 km.

(c)

(d)
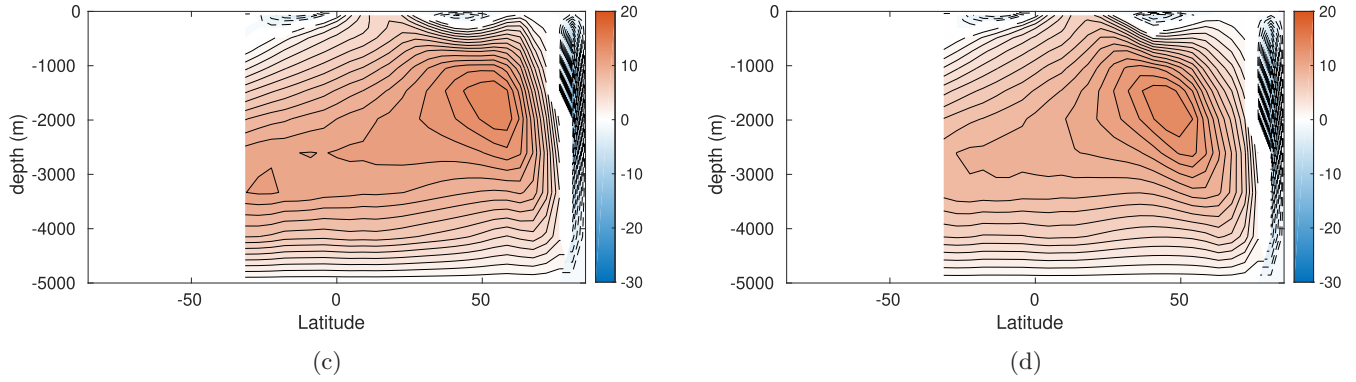
Fig. 3. (*Continued*)

Near the bifurcation L_2 some spatial variation emerges at the equator near Australia [Fig. 5(b)]. It appears that, in a transient computation, this point could mark the beginning of a transition to the ice-free branch.

For a better understanding of the destabilizing characteristics at L_1^a and L_2, we compute solutions of the generalized eigenvalue problem (49). At these bifurcations, an eigenvalue has been observed

to cross the imaginary axis. The atmospheric temperature component of the corresponding eigenvectors are shown in Fig. 6. The unstable eigenmodes show the pattern of unstable growth at the bifurcations. At L_1^a, a strong anomaly is present in the North Pacific near the Eurasian continent, which corresponds to a minor excursion of sea ice, visible in Fig. 4(a). This indicates that, for setup (a), this area is sensitive to perturbations and, hence,

(a)

(b)

(c)

(d)
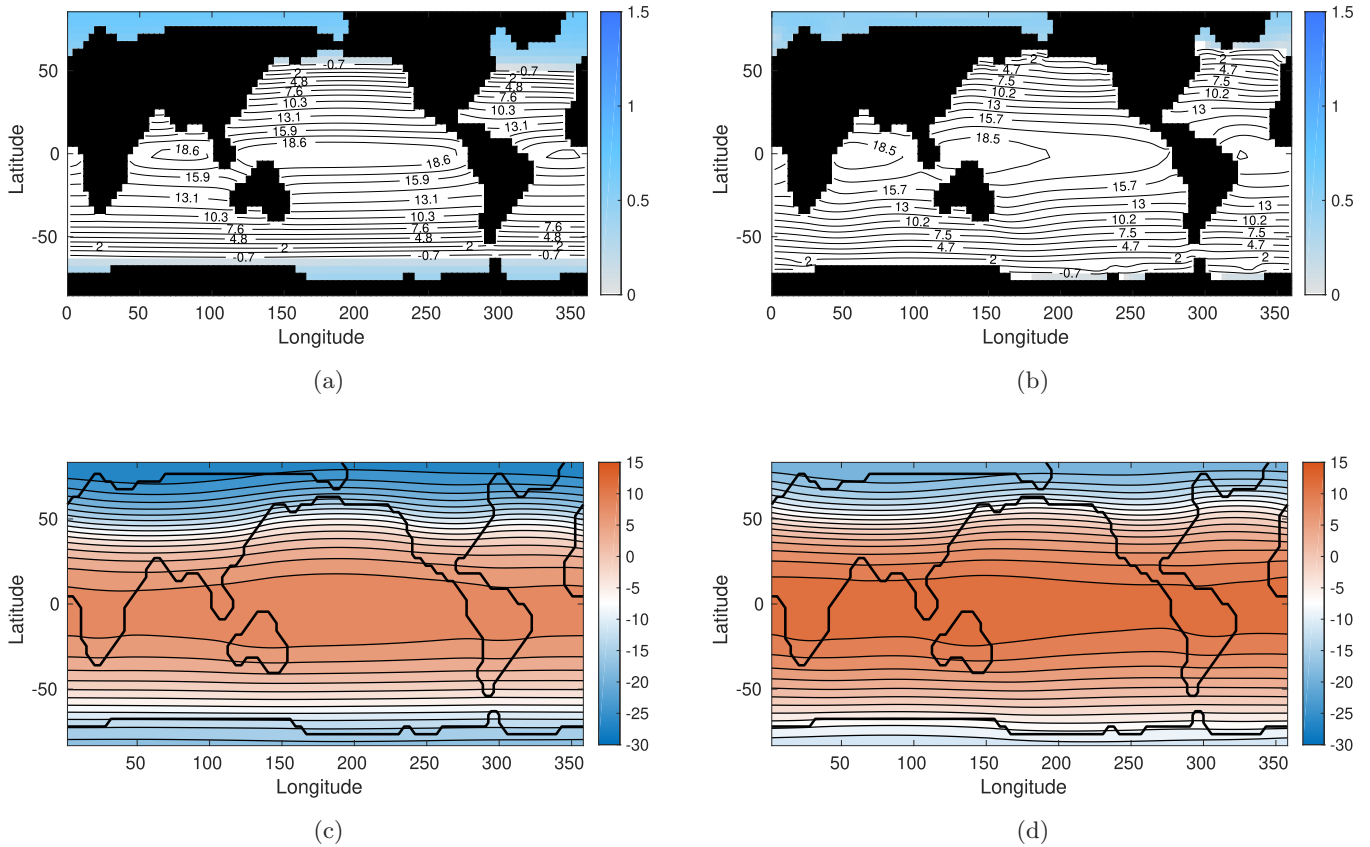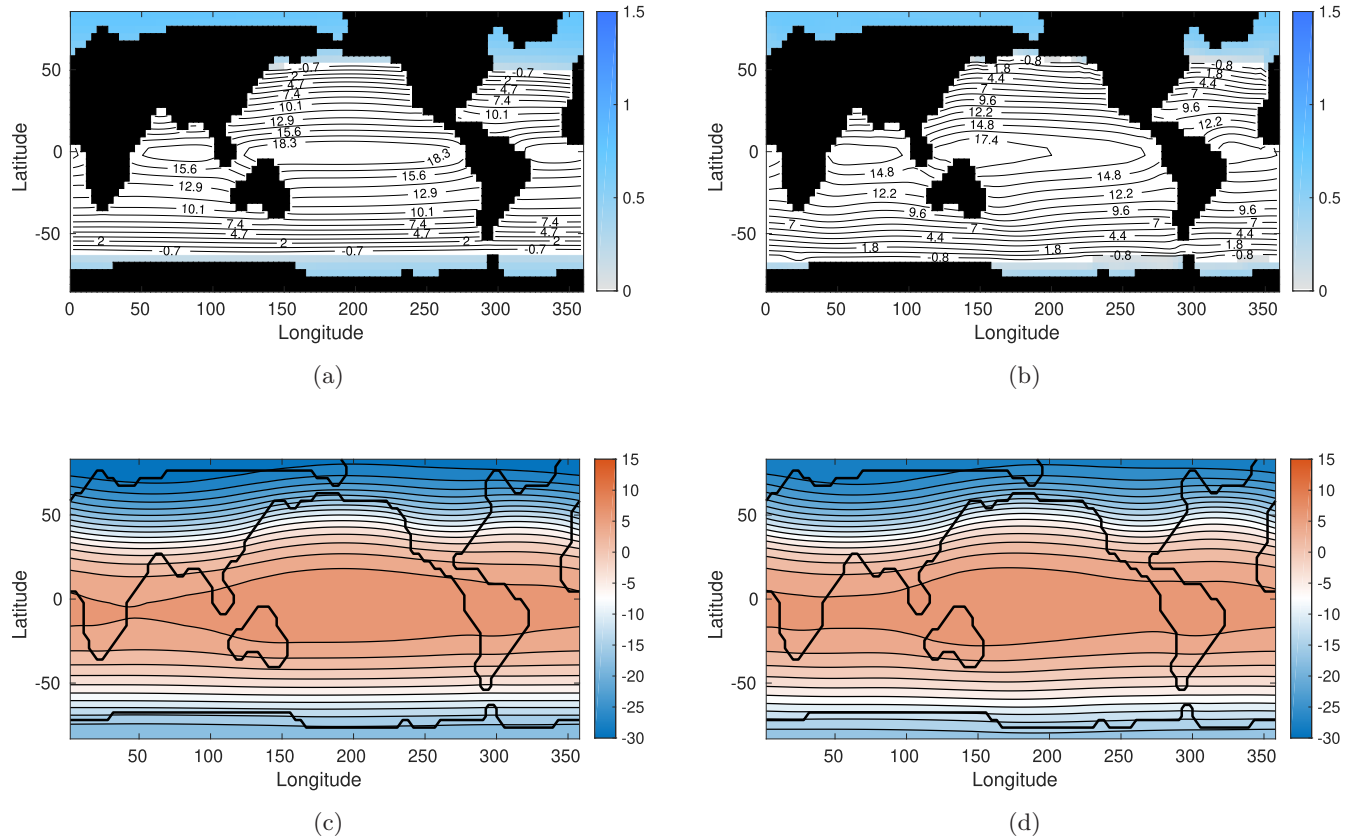
Fig. 4. (a) and (b) Sea ice thickness (colors, in m) and sea surface temperature (contours, in $^\circ$C), at the bifurcations (a) L_1^a and (b) L_1^b. (c) and (d) Atmospheric temperature (in $^\circ$C) at the bifurcations (c) L_1^a and (d) L_1^b.

(a)

(b)
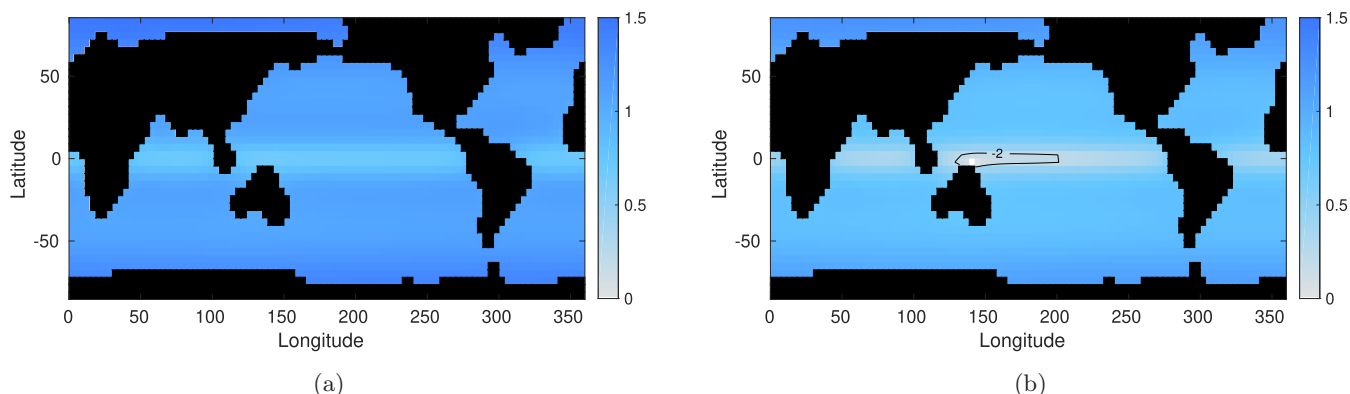
Fig. 5.   Sea ice thickness (colors, in m) and sea surface temperature (contours, in °C) at the points (a) P_2 and (b) L_2. Variation in sea surface temperature only occurs at the first opening in sea ice cover in (b).

(a)

(b)
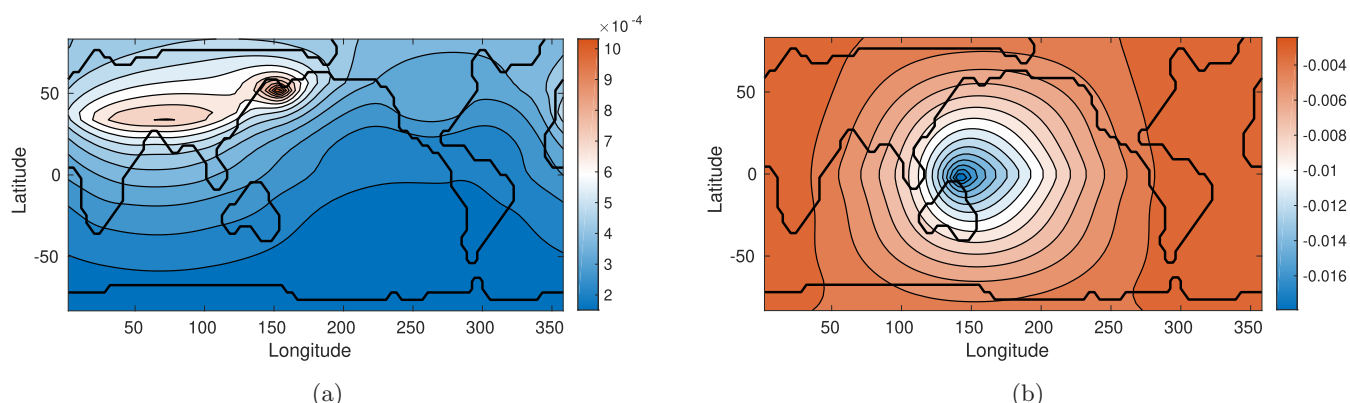
Fig. 6.   Atmospheric temperature component of the unstable eigenmode at (a) L_1^a and (b) L_2 in Fig. 1. Note that the sign and magnitude of the perturbation patterns are arbitrary.

a growth to a fully ice-covered ocean is likely to initiate here.

The destabilizing perturbation pattern at L_2 in Fig. 6(b) shows an anomaly at the equator near Australia. This area corresponds to the initial opening in the sea ice cover, visible in Fig. 5(b). The unstable eigenmode therefore confirms the suspicion that an opening in this region marks the start of a transition to the ice-free branch.

6.   Summary and Discussion

In this paper, we have presented the first fully-implicit Earth system model of intermediate complexity: the I-EMIC. The discretized model equations are explored using implicit time integration methods and continuation techniques. Both methods have been applied to investigate the snowball Earth hypothesis and the associated hysteresis structure. Time integrations were used to find steady states in the snowball Earth bifurcation

diagram, after which branches of equilibria were computed using numerical continuations. With this approach we were able to traverse a complex bifurcation structure associated with the ice-albedo feedback. The ability of the I-EMIC to perform these continuations has shown that the formulation of the coupled climate model is sufficiently smooth, i.e. it achieves a good Newton–Raphson convergence rate.

Several previous numerical parameter studies of global glaciation events [Abbot *et al.*, 2011; Voigt *et al.*, 2011] were limited to transient simulations and provided only a limited view of the snowball Earth bifurcation diagram. Now, with the I-EMIC, it is possible to follow stable and unstable branches precisely and thereby fully reveal the dynamical structure that underlies local and global hysteresis mechanisms. Furthermore, the I-EMIC allows novel insights into the patterns of variability around critical snowball Earth bifurcations using large-scale linear stability analyses. Dominant eigenvectors of the

Jacobian matrix, obtained at stable and unstable steady states, show the subtleties involved in the interaction between components of the Earth system that lead to a global instability mechanism.

Eigenvalue solutions, needed for the linear stability analysis of steady states within the I-EMIC, have so far been moderately successful. For model configurations without an ocean circulation, the computation of eigenvalues and eigenvectors is feasible for the fully coupled model. However, with wind- and density-driven flows in the ocean, the conditioning of the problem exceeds the current capabilities of the solving scheme. A particular bottleneck in the calculations is the preconditioning, which requires improvements in order to speed up continuations through densely packed fold bifurcations, and to be able to find eigenmodes of the fully dynamical problem at horizontal resolutions of 4° and finer.

The sections of the bifurcation diagram associated with sea ice growth, contain a dense structure of fold bifurcations due to sea ice-albedo feedbacks. From a tandem of local ice-albedo mechanisms, a large-scale bifurcation structure emerges. The choice of sea ice transition width ϵ affects the slope of the branches, but the intermediate bifurcations can only be removed by radically altering the basic radiation balance that governs the feedback. The dense occurrence of bifurcations is inherent to the discretized equations and, with the current sea ice formulation, only grid refinements may somewhat remedy this problem.

Additional modeling efforts are necessary to extend the atmospheric radiation balance, as the current formulation in the I-EMIC lacks a representation of greenhouse gases — most importantly CO_2. With an added carbon cycle in both the atmosphere and the ocean, the I-EMIC will acquire a new degree of realism, which, after meticulous testing and tuning, should make it suitable for efficient climate sensitivity analyses. Furthermore, the transition width in the sea ice mask equation should be a better approximation of the sea ice fraction within a grid cell. In order to compare with previous, transient based efforts [Voigt *et al.*, 2011], future snowball Earth experiments with the I-EMIC need to include a realistic, Marinoan topography. Additionally, to investigate the "Jormungand" state [Abbot *et al.*, 2011], the albedo parameterization in the I-EMIC needs to be expanded with a sea ice thickness dependency.

Apart from the snowball Earth problem, the I-EMIC has enormous potential in climate research as equilibrium states can be quickly computed versus parameters. This offers the possibility to tackle, for example, problems related to the Pleistocene Ice Ages, problems such as the Eocene-Oligocene transition and other deep-time scientific issues such as the climate in the Precambrium. The I-EMIC appears also very well suited to compute equilibrium climate states of other (exo)planets within (e.g. the climate on Titan) and outside of our solar system.

Acknowledgments

Code Availability

The I-EMIC project is being actively developed in collaboration with the Netherlands eScience Center (NLeSC) and is publicly available at https://github.com/nlesc-smcm/i-emic. The JDQZ generalized eigenvalue solver [Sleijpen *et al.*, 1996] used for this project is a templated `C++` port of the original code by Fokkema and van Gijzen. It can be found at https://github.com/erik808/jdqzpp.

References

Abbot, D. S., Voigt, A. & Koll, D. [2011] "The Jormungand global climate state and implications for Neoproterozoic glaciations," *J. Geophys. Res.* **116**, D18103.

Arakawa, A. & Lamb, V. [1977] "Computational design of the basic dynamical processes of the ucla general circulation model," *General Circulation Models of the Atmosphere*, Methods in Computational Physics: Advances in Research and Applications, Vol. 17 (Academic Press), pp. 173–265.

Boschi, R., Lucarini, V. & Pascale, S. [2012] "Bistability of the climate around the habitable zone: A thermodynamic investigation," *Icarus* **226**, 1724–1742.

Bryan, F. [1987] "Parameter sensitivity of primitive equation ocean general circulation models," *J. Phys. Oceanogr.* **17**, 970–985.

Budyko, M. I. [1969] "The effect of solar radiation variations on the climate of the Earth," *Tellus A* **21**, 611–619.

de Niet, A., Wubs, F., van Scheltinga, A. T. & Dijkstra, H. A. [2007] "A tailored solver for bifurcation analysis of ocean-climate models," *J. Comput. Phys.* **227**, 654–679.

den Toom, M., Dijkstra, H. A. & Wubs, F. W. [2011] "Spurious multiple equilibria introduced by convective adjustment," *Ocean Model.* **38**, 126–137.

Dijkstra, H. A., Oksuzoglu, H., Wubs, F. W. & Botta, E. F. F. [2001] "A fully implicit model of the three-dimensional thermohaline ocean circulation," *J. Comput. Phys.* **173**, 685–715.

Fanning, A. F. & Weaver, A. J. [1996] "An atmospheric energy-moisture balance model: Climatology, interpentadal climate change, and coupling to an ocean general circulation model," *J. Geophys. Res.* **101**, 15111.

Ghil, M. & Childress, S. [1987] *Topics in Geophysical Fluid Dynamics*: *Atmospheric Dynamics, Dynamo Theory, and Climate Dynamics* (Springer-Verlag, Berlin/Heidelberg/New York).

Gildor, H. & Tziperman, E. [2001] "A sea ice climate switch mechanism for the 100-kyr glacial cycles," *J. Geophys. Res.* **106**, 9117.

Hoffman, P. F., Abbot, D. S., Ashkenazy, Y., Benn, D. I., Brocks, J. J., Cohen, P. A., Cox, G. M., Creveling, J. R., Donnadieu, Y., Erwin, D. H., Fairchild, I. J., Ferreira, D., Goodman, J. C., Halverson, G. P., Jansen, M. F., Le Hir, G., Love, G. D., Macdonald, F. A., Maloof, A. C., Partin, C. A., Ramstein, G., Rose, B. E. J., Rose, C. V., Sadler, P. M., Tziperman, E., Voigt, A. & Warren, S. G. [2017] "Snowball earth climate dynamics and cryogenian geology-geobiology," *Sci. Adv.* **3**, e1600983.

Keller, H. B. [1977] "Numerical solution of bifurcation and nonlinear eigenvalue problems," *Applications of Bifurcation Theory* (*Proc. Advanced Sem.*, *Univ. Wisconsin*, *Madison*, *Wis.*, *1976*), Publ. Math. Res. Center, No. 38 (Academic Press, NY), pp. 359–384.

Kirschvink, J. L. [1992] "Late proterozoic low-latitude global glaciation: The snowball earth," *The Proterozoic Biosphere*: *A Multidisciplinary Study*, eds. Schopf, J. W., Klein, C. & Des Maris, D. (Cambridge University Press), pp. 51–52.

North, G. R., Cahalan, R. F. & Coakley, J. A. [1981] "Energy balance climate models," *Rev. Geophys.* **19**, 91.

Press, W. H., Teukolsky, S. A., Vetterling, W. T. & Flannery, B. P. [2007] *Numerical Recipes. The Art of Scientific Computing*, third edition (Cambridge University Press, Cambridge).

Saad, Y. [1993] "A flexible inner-outer preconditioned GMRES algorithm," *SIAM J. Sci. Comput.* **14**, 461–469.

Saad, Y. [2003] *Iterative Methods for Sparse Linear Systems*, second edition (SIAM).

Seydel, R. [2010] *Practical Bifurcation and Stability Analysis*, Interdisciplinary Applied Mathematics, Vol. 5 (Springer, NY).

Sleijpen, G. L. G., Booten, A. G. L., Fokkema, D. R. & Vorst, H. A. [1996] "Jacobi–Davidson type methods for generalized eigenproblems and polynomial eigenproblems," *BIT Numer. Math.* **36**, 595–633.

Thies, J., Wubs, F. & Dijkstra, H. A. [2009] "Bifurcation analysis of 3D ocean flows using a parallel fully-implicit ocean model," *Ocean Model.* **30**, 287–297.

Voigt, A., Abbot, D. S., Pierrehumbert, R. T. & Marotzke, J. [2011] "Initiation of a Marinoan Snowball Earth in a state-of-the-art atmosphere-ocean general circulation model," *Clim. Past* **7**, 249–263.

Weaver, A. J., Eby, M., Wiebe, E. C., Bitz, C. M., Duffy, P. B., Ewen, T. L., Fanning, A. F., Holland, M. M., MacFadyen, A., Matthews, H. D., Meissner, K. J., Saenko, O., Schmittner, A., Wang, H. & Yoshimori, M. [2001] "The UVic earth system climate model: Model description, climatology, and applications to past, present and future climates," *Atmosph. Ocean* **39**, 361–428.

Wubs, F. W., de Niet, A. C. & Dijkstra, H. A. [2006] "The performance of implicit ocean models on B- and C-grids," *J. Comput. Phys.* **211**, 210–228.

Yang, J., Peltier, W. R. & Hu, Y. [2012a] "The initiation of modern soft and hard Snowball Earth climates in CCSM4," *Clim. Past* **8**, 907–918.

Yang, J., Peltier, W. R. & Hu, Y. [2012b] "The initiation of modern 'soft snowball' and 'hard snowball' climates in CCSM3. Part I: The influences of solar luminosity, CO2 concentration, and the sea ice/snow Albedo parameterization," *J. Clim.* **25**, 2711–2736.

Appendix A

Model Overview and Matrix Formulation

In this section, we provide an overview of the I-EMIC's equations and follow with the structure of the associated Jacobian matrix.

$$
\frac{Du}{dt} - \frac{uv\tan\theta}{r_0} - 2\Omega v\sin\theta
$$

$$
= -\frac{1}{\rho_o r_0 \cos\theta}\frac{\partial p}{\partial \phi} + A_V\frac{\partial^2 u}{\partial z^2}
$$

$$
+ A_H \mathcal{V}(u,v) + Q_\tau^\phi, \tag{A.1}
$$

$$\frac{Dv}{dt} + \frac{u^2 \tan\theta}{r_0} + 2\Omega u \sin\theta$$

$$= -\frac{1}{\rho_o r_0}\frac{\partial p}{\partial \theta} + A_V \frac{\partial^2 v}{\partial z^2}$$

$$+ A_H \mathcal{V}(v, -u) + Q_\tau^\theta, \qquad (\text{A.2})$$

$$0 = -\frac{\partial p}{\partial z} - \rho_o g(1 - \alpha_T(T - T_0)$$

$$+ \alpha_S(S - S_0)), \qquad (\text{A.3})$$

$$0 = \frac{\partial w}{\partial z} + \frac{1}{r_0 \cos\theta}\left(\frac{\partial u}{\partial \phi} + \frac{\partial(v\cos\theta)}{\partial\theta}\right), \qquad (\text{A.4})$$

$$\frac{DT}{dt} = \nabla_h \cdot (K_H \nabla_h T) + \frac{\partial}{\partial z}\left(K_V \frac{\partial T}{\partial z}\right)$$

$$+ \text{ca}(T) + Q_T, \qquad (\text{A.5})$$

$$\frac{DS}{dt} = \nabla_h \cdot (K_H \nabla_h S) + \frac{\partial}{\partial z}\left(K_V \frac{\partial S}{\partial z}\right)$$

$$+ \text{ca}(S) + Q_S, \qquad (\text{A.6})$$

$$\rho_a H_a C_{pa}\frac{\partial T^a}{\partial t} = Q_T - Q_{LW} + Q_{SW}$$

$$+ Q_{SH} + Q_{LH}, \qquad (\text{A.7})$$

$$\rho_a H_q \frac{\partial q}{\partial t} = \rho_a H_q \nabla_h \cdot (\kappa \nabla_h q) + \rho_o(E - P), \qquad (\text{A.8})$$

$$\frac{\partial \alpha}{\partial t} = \begin{cases} \tau_f^{-1}(\alpha_0 + \Delta\alpha f(T^l, P) - \alpha) & \text{if } M = 1, \\ \tau_c^{-1}(\alpha_0 + \Delta\alpha M^{si} - \alpha) & \text{if } M = 0, \end{cases} \qquad (\text{A.9})$$

$$0 = \frac{d(\phi,\theta)}{A}\int E dA - P, \qquad (\text{A.10})$$

$$\rho_i L_f \frac{\partial H}{\partial t} = Q_T^{os} - Q_T^{sa} - \rho_o L_f E, \qquad (\text{A.11})$$

$$0 = Q_T^{sa} - Q_{SW} + Q_{SH} + Q_{LH}, \qquad (\text{A.12})$$

$$0 = M^{si} - \frac{1}{2}\left[1 + \tanh\left(\frac{H - \tau_s}{\epsilon}\right)\right], \qquad (\text{A.13})$$

$$0 = T^f - T^i + \frac{Q_T^{sa} H}{I_c}, \qquad (\text{A.14})$$

$$0 = \int M^{si}(Q_S^{os} - (E^i - P))dA - \gamma A, \qquad (\text{A.15})$$

where a linear equation of state is substituted in the hydrostatic equation (A.3) and

$$\frac{D}{dt} = \frac{\partial}{\partial t} + \frac{u}{r_0 \cos\theta}\frac{\partial}{\partial\phi} + \frac{v}{r_0}\frac{\partial}{\partial\theta} + w\frac{\partial}{\partial z}, \qquad (\text{A.16})$$

$$\mathcal{V}(f,g) = \nabla_h^2 f - \frac{f}{r_0^2 \cos^2\theta} - \frac{2\sin\theta}{r_0^2 \cos^2\theta}\frac{\partial g}{\partial\phi}, \qquad (\text{A.17})$$

$$\nabla_h f = \left(\frac{1}{r_0 \cos\theta}\frac{\partial f}{\partial\phi}, \frac{1}{r_0}\frac{\partial f}{\partial\theta}\right)^T, \qquad (\text{A.18})$$

$$\nabla_h^2 = \nabla_h \cdot \nabla_h. \qquad (\text{A.19})$$

Boundary conditions for the ocean equations are given by

$$\phi = \phi_W, \phi_E:$$

$$u = v = w = 0, \quad \frac{\partial T}{\partial\phi} = \frac{\partial S}{\partial\phi} = 0, \qquad (\text{A.20})$$

$$\theta = \theta_S, \theta_N:$$

$$u = v = w = 0, \quad \frac{\partial T}{\partial\theta} = \frac{\partial S}{\partial\theta} = 0, \qquad (\text{A.21})$$

$$z = -D, 0:$$

$$\frac{\partial u}{\partial z} = \frac{\partial v}{\partial z} = 0, \quad w = 0, \quad \frac{\partial T}{\partial z} = \frac{\partial S}{\partial z} = 0. \qquad (\text{A.22})$$

Similarly, for the atmosphere equations we require

$$\phi = \phi_W, \phi_E: \quad \frac{\partial T^a}{\partial\phi} = \frac{\partial q}{\partial\phi} = 0, \qquad (\text{A.23})$$

$$\theta = \theta_S, \theta_N: \quad \frac{\partial T^a}{\partial\theta} = \frac{\partial q}{\partial\theta} = 0. \qquad (\text{A.24})$$

Spatial discretization gives a system of differential-algebraic equations (DAEs, see Sec. 4):

$$B\dot{\mathbf{x}} = F(\mathbf{x}, \lambda). \qquad (\text{A.25})$$

Newton–Raphson iterations are necessary to compute orbits and steady states of (A.25) implicitly. This root-finding procedure requires the solution of

$$J\mathbf{x} = \mathbf{b}, \qquad (\text{A.26})$$

where $\mathbf{x}, \mathbf{b} \in \mathbb{R}^n$ are vectors in the state space of the dynamical system (A.25) and $J \in \mathbb{R}^{n \times n}$ is the Jacobian matrix, i.e. the derivative of F with respect to the state. One way to summarize the couplings between the submodels is through expanding the

matrix-vector product in (A.26):

$$
\begin{bmatrix}
J_{uv} & E_w & G_p^{uv} \\
 & 0 & G_p^w & B_{TS} \\
D_{uv} & D_w & 0 \\
B_{uv} & B_w & & J_{TS} & C_{Tq}^{TS} & C_\alpha^{TS} & \mathbf{c}_P^{TS} & & C_{QT}^{TS} & C_M^{TS} & \mathbf{c}_\gamma^{TS} \\
 & & & C_{TS}^{Tq} & J_{Tq} & C_\alpha^{Tq} & \mathbf{c}_P^{Tq} & & C_{QT}^{Tq} & C_M^{Tq} \\
 & & & & C_{Tq}^\alpha & J_\alpha & \mathbf{c}_P^\alpha & & & C_M^\alpha \\
 & & & \mathbf{p}_{TS}^\mathsf{T} & \mathbf{p}_{Tq}^\mathsf{T} & & -1 & & \mathbf{p}_{QT}^\mathsf{T} & \mathbf{p}_M^\mathsf{T} \\
 & & & C_{TS}^H & C_{Tq}^H & & & 0 & C_{QT}^H \\
 & & & C_{TS}^{QT} & C_{Tq}^{QT} & C_\alpha^{QT} & & C_H^{QT} & J_{QT} \\
 & & & & & & & C_H^M & & J_M \\
 & & & \boldsymbol{\gamma}_{TS}^\mathsf{T} & \boldsymbol{\gamma}_{Tq}^\mathsf{T} & & \gamma_P & & \boldsymbol{\gamma}_{QT}^\mathsf{T} & \boldsymbol{\gamma}_M^\mathsf{T} & -A
\end{bmatrix}
\begin{bmatrix}
\mathbf{x}_{uv} \\
\mathbf{x}_w \\
\mathbf{x}_p \\
\mathbf{x}_{TS} \\
\mathbf{x}_{Tq} \\
\mathbf{x}_\alpha \\
\mathbf{x}_P \\
\mathbf{x}_H \\
\mathbf{x}_{QT} \\
\mathbf{x}_M \\
\mathbf{x}_\gamma
\end{bmatrix}.
\qquad (A.27)
$$

The ocean model derivatives determine the first four rows, atmosphere derivatives are present in the next three rows and the remaining four rows are given by sea ice derivatives. The diagonal blocks J_{uv} and J_{TS} are convection-diffusion operators, where J_{uv} also contains a Coriolis component. The J_{Tq} block is a plain diffusion operator and the remaining diagonal blocks do not differentiate spatial discretizations. For the internal off-diagonal ocean model blocks we use the notation of [de Niet *et al.*, 2007]. The matrix E_w contains the coupling of the horizontal momentum equations with w through the material derivative, G_p^* are gradient operators that act on the pressure field, D_* are divergence operators for the velocities and heat and salinity dependencies are present in the B_* blocks. The remaining couplings are represented by the coupling blocks C_y^x. For instance, the derivative of the ocean model T and S equations with respect to reflectivity α is given by C_α^{TS}. Integral equations are given by transposed vectors.

The expanded matrix-vector product (A.27) shows how the oceanic heat and salinity equations provide the coupling interface in the I-EMIC. If we would ignore any circulation in the ocean, the Jacobian can be reduced to the shaded part in (A.27), ignoring the first three rows and columns. The sparsity structure of this reduced problem is shown in Fig. 7.

Fig. 7. Sparsity pattern of the shaded blocks in (A.27) that are relevant for the coupling between the submodels using a Jacobian matrix that is based on a coarse aquaplanet problem (no continents). Dashed lines show the separation of blocks using the ordering in (A.27), starting at the diagonal block J_{TS} (top left corner) and ending at the final element $-A$ (lower right corner). Horizontal red lines mark the auxiliary integral equations for P (A.10) and γ (A.15) and vertical red lines are the dependencies on these auxiliary unknowns. Note that two other integral equations are present in the blocks J_{TS} and J_{Tq}. These are integral constraints that require conservation of humidity and salinity.

Appendix B
Parameter Values

Table B.1.   Ocean parameters that are used for the continuation runs in Sec. 5.

ρ_o	$1024\,\mathrm{kg\,m^{-3}}$	Reference water density
H_o	$5.0 \times 10^3\,\mathrm{m}$	Maximum ocean depth
H_m	$72\,\mathrm{m}$	Ocean upper layer depth
C_{po}	$4.1 \times 10^3\,\mathrm{J\,(kg\,K)^{-1}}$	Specific heat of sea water
A_H	$1.6 \times 10^7\,\mathrm{m^2\,s^{-1}}$	Horizontal eddy viscosity
A_V	$1.0 \times 10^{-3}\,\mathrm{m^2\,s^{-1}}$	Vertical eddy viscosity
K_H	$1.0 \times 10^3\,\mathrm{m^2\,s^{-1}}$	Horizontal diffusivity of heat and salt
K_V	$1.0 \times 10^{-4}\,\mathrm{m^2\,s^{-1}}$	Vertical diffusivity of heat and salt
α_T	$1.0 \times 10^{-4}\,\mathrm{K^{-1}}$	Thermal expansion coefficient
α_S	$7.6 \times 10^{-4}\,\mathrm{psu^{-1}}$	Haline contraction coefficient

Table B.2.   Atmospheric temperature and specific humidity parameter values.

ρ_a	$1.25\,\mathrm{kg\,m^{-3}}$	Atmospheric density
H_a	$8.4 \times 10^3\,\mathrm{m}$	Atmospheric scale height
H_q	$1.8 \times 10^3\,\mathrm{m}$	Specific humidity scale height
C_{pa}	$10^3\,\mathrm{J\,(kg\,K)^{-1}}$	Specific heat of air
C_E	1.3×10^{-3}	Dalton number
C_H	1.22×10^{-3}	Stanton number ($\approx 0.94 C_E$)
$|V_a|$	$8.5\,\mathrm{m\,s^{-1}}$	Mean surface wind speed
D_0	$3.1 \times 10^6\,\mathrm{m^2\,s^{-1}}$	Constant eddy diffusivity
κ	$1.0 \times 10^6\,\mathrm{m^2\,s^{-1}}$	Constant eddy diffusivity
$1 - C_0$	0.57	Atmospheric absorption coefficient
Σ_0	$1.36 \times 10^3\,\mathrm{W\,m^{-2}}$	Solar constant
A	$216\,\mathrm{W\,m^{-2}}$	Q_{LW} offset
B	$1.5\,\mathrm{W\,m^{-2}\,K^{-1}}$	Q_{LW} temperature sensitivity
L_v	$2.5 \times 10^6\,\mathrm{J\,kg^{-1}}$	Latent heat of vaporization
μ	$13\,\mathrm{W\,m^{-2}\,K^{-1}}$	Exchange coefficient
η	$1.35 \times 10^{-5}\,\mathrm{m\,s^{-1}}$	Evaporation scale

Table B.3.   Summary of the parameters used for the implicit sea ice model.

$C_{po} = 4.1 \times 10^3\,\mathrm{J\,(kg\,K)^{-1}}$	Specific heat of sea water
$C_s = 0.0058$	Relaxation parameter
$u_\tau = 0.02\,\mathrm{m\,s^{-1}}$	Skin friction velocity
$I_c = 2.166\,\mathrm{W\,m^{-1}\,K^{-1}}$	Thermal conductivity of ice
$L_f = 3.347 \times 10^5\,\mathrm{J\,kg^{-1}}$	Latent heat of fusion of ice
$L_s = 2.835 \times 10^6\,\mathrm{J\,kg^{-1}}$	Latent heat of sublimation of ice
$\tau_s = 0.3\,\mathrm{m}$	Threshold ice thickness
$\epsilon = 0.6\,\mathrm{m}$	Transition width

Table B.4.   Coefficients for the computation of the saturation specific humidity $q_{\mathrm{sat}}(T)$ above ocean and sea ice points.

$c_1 = 3.8 \times 10^{-3}\,\mathrm{kg\,kg^{-1}}$	$c_2 = 21.87$
$c_3 = 265.5\,\mathrm{K}$	$c_4 = 17.67$
$c_5 = 243.5\,\mathrm{K}$	